Nanoscale heterogeneity induced by nonmagnetic Zn dopants in the quantum critical metal math xmlns="http://www.w3.org/1998/Math/MathML">msub>mi>CeCoIn/mi>mn>5/mn>/msub>/math>: math xmlns="http://www.w3.org/1998/Math/MathML">mmultiscripts>mi>In/mi>mprescripts>/mprescripts>none>/none>mn>115/mn>/mmultiscripts>/math> NQR/NMR and math xmlns="http://www.w3.org/1998/Math/MathML">mmultiscripts>mi>Co/mi>mprescripts>/mprescripts>none>/none>mn>59/mn>/mmultiscripts>/math> NMR study

H. Sakai, Y. Tokunaga, S. Kambe, J.-X. Zhu, F. Ronning, J. D. Thompson, S. K. Ramakrishna, A. P. Reyes, K. Suzuki, Y. Oshima, and M. Yokoyama

Phys. Rev. B **104**, 085106 — Published 5 August 2021

DOI: 10.1103/PhysRevB.104.085106

Nano-scale heterogeneity induced by non-magnetic Zn dopants in a quantum critical metal CeCoIn$_5$: ^{115}In NQR/NMR and ^{59}Co NMR Study

H. Sakai,[*] Y. Tokunaga, and S. Kambe
Advanced Science Research Center, Japan Atomic Energy Agency, Tokai, Ibaraki, 319-1195, Japan.

J.-X. Zhu, F. Ronning, and J. D. Thompson
Los Alamos National Laboratory, Los Alamos, New Mexico 87545, USA

S. K. Ramakrishna and A. P. Reyes
National High Magnetic Field Laboratory, Florida State University, Tallahassee, Florida 32310, USA.

K. Suzuki, Y. Oshima, and M. Yokoyama
Faculty of Science, Ibaraki University, Mito, Ibaraki 310-8512, Japan.
(Dated: July 21, 2021)

Antiferromagnetism in a prototypical quantum critical metal CeCoIn$_5$ is known to be induced by slight substitutions of non-magnetic Zn atoms for In. In nominally 7% Zn substituted CeCoIn$_5$, an antiferromagnetic (AFM) state coexists with heavy fermion superconductivity. Heterogeneity of the electronic states is investigated in Zn doped CeCoIn$_5$ by means of nuclear quadrupole and magnetic resonances (NQR and NMR). Site-dependent NQR relaxation rates $1/T_1$ indicate that the AFM state is locally nucleated around Zn substituents in the matrix of a heavy fermion state, and percolates through the bulk at the AFM transition temperature T_{N}. At lower temperatures, an anisotropic superconducting (SC) gap below the SC transition temperature T_{c}, and the SC state permeates through the AFM regions via a SC proximity effect. Applying an external magnetic field induces a spin-flop transition near 5 T, reducing the volume of the AFM regions. Consequently, a short ranged inhomogeneous AFM state survives and coexists with a paramagnetic Fermi liquid state at high fields.

I. INTRODUCTION

Slight doping of elements into semiconductors, magnets, or superconductors is often performed to achieve functional improvements. If the role of dopants is clarified at the microscopic level, a beneficial direction can be indicated for enhanced functionality. Especially, in heavy fermion systems, chemical doping can be utilized to access a quantum critical point (QCP) [1–3]. Experimentally, quite often it is difficult to clarify the role of dopants microscopically. If the material in pure form is at or very close to a QCP, the role of substitutions can be tested at the microscopic level with a small number of substituents. The heavy fermion compound CeCoIn$_5$ is one of the few materials in which this test might be made.

It belongs to the CeTIn$_5$ (T=Co, Rh, Ir) family, and is known to lie in close proximity to an antiferromagnetic (AFM) QCP at ambient pressure [4, 5]. Non-magnetic substitutions for the ligand In [$5s^25p$] sites in CeCoIn$_5$ by Sn and Cd elements nominally dope electrons (Sn) and holes (Cd) into CeCoIn$_5$. Recently, a qualitative difference in local electronic environments around Sn and Cd substituents has been probed by nuclear quadrupole resonance (NQR) [6]. In the case of Sn [$5s^25p^2$] substitution, AFM fluctuations are uniformly suppressed as the system is driven away from the AFM QCP [6–9]. In this case, the c–f hybridization is also found to be strengthened rather homogeneously. On the other hand, a small amount of Cd [$5s^2$] substitution for In, induces long-range AFM order [10]. One may think that the long-range AFM state might be induced by“negative” chemical pressure. With applying “positive” pressure to the induced AFM state, however, the fluctuations and the signatures in electrical transport properties at this pressure-induced AFM QCP are absent [11]. A recent study of Cd doped CeIrIn$_5$ draws the same conclusion [12]. From a microscopic view [6], Cd substitutions produce a heterogeneous electronic state where Cd substituents enhance AFM behavior by inducing unscreened localized moments in their immediate vicinity, but the bulk electronic state far from the Cd substituents is the same as in the pure CeCoIn$_5$.

Such a dichotomy in the response of CeCoIn$_5$ to Sn and Cd substitutions is also observed by soft-x-ray absorption spectroscopy [13]. While the majority of $4f$ wave function remains globally unaltered by Cd (hole doping) substitutions, the shape of $4f$ orbitals become oblate and the c–f hybridization becomes stronger with Sn (electron doping) substitutions. Very recently, further evidence of this dichotomy was suggested by Hall resistivity measurements [14], which implied that the carrier density of the conduction and itinerant $4f$ electrons remained constant with Cd doping while it is suddenly changed by slight Sn doping.

In this paper, we provide evidence for a nano-scaled heterogeneous electronic state in CeCoIn$_5$ induced by

---

[*] E-mail: sakai.hironori@jaea.go.jp

hole-doping on the ligand sites, using Zn as the dopant. In the solid solution $\mathrm{CeCo(In}_{1-x}\mathrm{Zn}_x)_5$ ($x \leq 0.07$), T_c is gradually suppressed by Zn doping, and the AFM transition with the transition temperature $T_\mathrm{N} \simeq 2.2$ K is induced for nominal $x \geq 0.05$ [15, 16], as in the Cd-doped case. At nominal $x = 0.07$ Zn doping, superconductivity emerges at the onset temperature $T_\mathrm{c}^{onset} \simeq 1.4$ K, and a bulk superconducting (SC) state is established at $T_\mathrm{c} \simeq 1.2$ K, which is below long-range AFM ordering at $T_\mathrm{N} \simeq 2.2$ K. In the nominally 7% Zn doped system, a new high field AFM (HF-AFM) phase has been also reported to appear above $\mu_0 H_0 = 5$ T below ~1.5 K [17]. We will show that the HF-AFM phase is a consequence of the heterogeneous electronic state induced by the Zn doping.

In Sec. II, the experimental details are provided. Section III consists of six subsections. In Sec. III A, we present NQR results under zero magnetic field. In Sec. III B, the NQR spectral assignment is carried out by comparison with the calculated NQR spectra using a 2×2×2 superlattice. The site-to-site NQR relaxation rate in the paramagnetic (PM) state indicates local electronic heterogeneity. In Sec. III C, the low-field AFM structure is discussed based on NQR and nuclear magnetic resonance (NMR) spectra of the two crystallographically different In(1) and In(2) sites under zero external field. In Sec. III D, we give detailed results of NQR $1/T_1$ measurements: the bulk electronic state in the PM state is equivalent with that in the undoped material, but spectra near the Zn dopants exhibits local spin excitations. The results of NQR $1/T_1$ in the AFM and SC states are also shown. In Sec. III E, NMR results under applied external magnetic fields are shown. ^{59}Co-NMR and ^{115}In-NMR data for In(1) and In(2) give information on the low-field and HF-AFM structures. In Sec. III F, the microscopic picture of the heterogeneous electronic state in 7% Zn doped CeCoIn_5 is drawn based on the NQR/NMR results. Finally, a summary of the microscopic study is presented in Sec. IV.

II. EXPERIMENT

Single crystals of $\mathrm{CeCo(In}_{1-x}\mathrm{Zn}_x)_5$ with $x = 0$, 0.025, and 0.07 were grown by means of the indium-flux technique [15, 16]. In this paper, we use the nominal x values for Zn doped samples for simplicity. It is, however, noted that the estimated Zn amounts were roughly 35% (±20%) of the nominal x values obtained from the starting ratio of ligand atoms [15]. For example, the actual Zn concentration y was estimated to be about 0.025 for a nominal $x = 0.07$ sample by energy dispersive X-ray spectroscopy (EDS) measurement. Such a compositional deviation from the nominal ratio occurs in isostructural $\mathrm{CeCo(In,Cd)}_5$, $\mathrm{CeCo(In,Hg)}_5$, $\mathrm{CeCo(In,Sn)}_5$, and $\mathrm{CeRh(In,Sn)}_5$ alloys [7, 10, 18]. If necessary, whether the doping level is nominal (x) or actual (y) will be stated in parentheses.

Crystals for NQR/NMR measurements were selected from the same batches used for magnetic susceptibility, electrical resistivity, and specific-heat measurements [15–17]. Although there was a little sample dependence on the low-temperature ordered phases for each x within a batch, the transition temperatures of each piece were checked by resistivity measurements. For each NQR/NMR experiment, a single crystal with a typical dimension of $3 \times 3 \times 0.2$ mm^3 was tightly wound by a thin copper wire with a diameter 50–150 μm to form a solenoid coil for radio frequency (r.f.) excitations. The coil with the sample was mounted on an NQR/NMR probe with two variable capacitors to tune the resonance frequencies and to match impedance of the r.f. circuit. The NQR/NMR experiments were carried out in ^{4}He, ^{3}He, or ^{3}He-^{4}He cryostats and were performed using a phase-coherent, pulsed spectrometer. External magnetic fields (H_0) were applied using a highly-homogeneous NMR grade SC magnet. To form the nuclear spin echoes, $90^\circ - 180^\circ$ conditions were used with a first pulse duration of 20–30 μsec and with the smallest possible power to avoid r.f. heating of the sample. The separation τ between first and second pulses was typically 30–50 μsec. Frequency-swept spectra were measured by tuning the r.f. network at each frequency, in steps of 10–50 kHz. To obtain the entire NMR spectrum, fast-Fourier-transform (FFT) spectra at the respective frequencies were overlapped and summed.

Using conventional notation, the quadrupole frequency parameter is defined as $\nu_\mathrm{Q} \equiv \frac{3e^2qQ}{2I(2I-1)h}$, where eQ is the nuclear quadrupolar moment, I is the nuclear spin quantum number, and $eq \equiv V_{ZZ}$ is the principal component of the electric field gradient (EFG) tensor. The EFG asymmetry parameter is defined as $\eta \equiv \frac{|V_{YY}-V_{XX}|}{|V_{ZZ}|}$. The ^{115}In NQR spectrum of $I = 9/2$ for CeCoIn_5 consists of 4 lines for In(1) sites with an equal separation of $\nu_\mathrm{Q} = 8.17$ MHz and $\eta = 0$, and 4 unequally-separated lines for In(2) sites whose positions give $\nu_\mathrm{Q} = 15.5$ MHz and $\eta = 0.39$ [19]. Similarly, the EFG parameters for ^{59}Co with $I = 7/2$ in CeCoIn_5 are ν_Q=0.113 MHz and η=0. [19]

EFGs were calculated by density functional theory (DFT) [8] assuming 2.5% Sn, Cd, or Zn doping in a $2 \times 2 \times 2$ supercell. The DFT calculations were performed using the WIEN2K code [20] with the exchange correlation functional of Perdew, Burke and Ernzerhof under the generalized gradient approximation [21]. Spin orbit coupling was included via a second order variational scheme.

The nuclear spin-lattice relaxation time T_1 was measured using the inversion-recovery method with a π-pulse. To evaluate NQR T_1 for In nuclei, each recovery curve $R(t)$ was fit by the recovery function for the $4\nu_\mathrm{Q}$ ($|\pm\frac{9}{2}\rangle \leftrightarrow |\pm\frac{7}{2}\rangle$) transition line of $I = 9/2$ with a single T_1: $R(t) \propto (4/33)\exp(-3t/T_1) + (80/143)\exp(-10t/T_1) + (49/165)\exp(-21t/T_1) + (16/715)\exp(-36t/T_1)$, which is derived assuming the asymmetry parameter $\eta = 0$. In the case of finite η, the recovery function was cal-

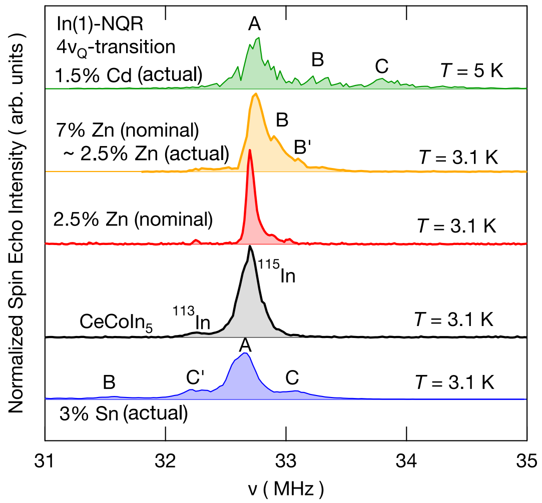

FIG. 1. In(1)–$4\nu_{\mathrm{Q}}$ NQR spectra for 3% Sn (actual) doped [6], non-doped, 2.5% Zn (nominal), 7% Zn (nominal) and 1.5% Cd doped (actual) CeCoIn$_5$ [6, 23] in the PM (normal) state. The upper case labels A, B, B', C, and C' indicate the respective spectral positions.

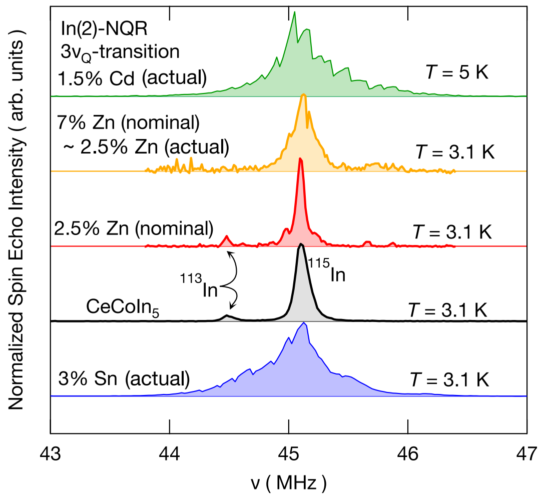

FIG. 2. In(2)–$3\nu_{\mathrm{Q}}$ NQR spectra for 3% Sn (actual) doped [6], non-doped, 2.5% Zn (nominal), 7% Zn (nominal) and 1.5% Cd (actual) doped CeCoIn$_5$ [6, 23] in the PM (normal) state.

culated by numerically diagonalizing the master equation for nuclear relaxation [22]. As for T_1 of ^{59}Co NMR under H_0, $R(t)$ for the central transition of $I = 7/2$ of the form $(1/84)\exp(-t/T_1) + (3/44)\exp(-6t/T_1) + (75/364)\exp(-15t/T_1) + (1225/1716)\exp(-28t/T_1)$ was used.

III. RESULTS

A. ^{115}In NQR spectra

CeCoIn$_5$ forms in the tetragonal HoCoGa$_5$-type structure ($P4/mmm$) with two crystallographically inequivalent In sites denoted as In(1) ($4/mmm$) and In(2)($2mm$). The Ce sites are surrounded on all sides by 4 nearest neighbor (NN) In(1) (at 3.26 Å) and 8 NN In(2) atoms (at 3.28 Å) [24]. Figure 1 shows the NQR spectra of the $4\nu_{\mathrm{Q}}$ transition ($|\pm\frac{9}{2}\rangle \leftrightarrow |\pm\frac{7}{2}\rangle$) for the In(1) sites in the PM state of 3% Sn (actual) doped [6], non-doped, 2.5% Zn (nominal), 7% Zn (nominal) and 1.5% Cd (actual) doped CeCoIn$_5$ [6, 23]. In the case of pure CeCoIn$_5$, since all the In(1) nuclei experience an equivalent EFG from the surrounding electrons, there is a single peak in the PM state for In(1) NQR. A minor peak on the left-hand side of the ^{115}In(1)-$4\nu_{\mathrm{Q}}$ line of pure CeCoIn$_5$, corresponds to the NQR transition of ^{113}In(1) nuclei with a small natural abundance of 4.7% and an almost similar nuclear quadrupolar moment, $^{113}Q/^{115}Q = 0.983$.

In the PM state of doped CeCoIn$_5$, the $4\nu_{\mathrm{Q}}$ line for In(1) splits into a main peak (A) and several subpeaks labeled B, B', C, and C'. ^{113}In(1) NQR signals in the doped samples were too small to be clearly observed. For the In(1) NQR spectra in the 2.5% and 7% Zn doped cases, the B and B' satellite peaks appear on the right-hand side of the main A peak. Since the satellites in the Zn doped case are close to each other, the distribution of EFG is somewhat narrower than in the 1.5% Cd doped case.

On the other hand, Fig. 2 shows the NQR spectra of the $3\nu_{\mathrm{Q}}$ transition ($|\pm\frac{7}{2}\rangle \leftrightarrow |\pm\frac{5}{2}\rangle$) for the In(2) sites in the PM state of the doped and non-doped CeCoIn$_5$. As in the In(1) case, In(2) NQR on the pure compound produces a single peak for all ^{115}In and ^{113}In nuclei. The spectral shapes of the In(2) NQR in doped CeCoIn$_5$ are rather featureless, i.e., those appear to be just broadened, although the broadening in the Zn doped case is a bit smaller than those in the 1.5% Cd and 3% Sn doped cases.

B. Spectral assignment of ^{115}In NQR

The NQR spectra for the $4\nu_{\mathrm{Q}}$ transition of In(1) and the $3\nu_{\mathrm{Q}}$ transition of In(2) of doped CeCoIn$_5$ are simulated using a 2×2×2 supercell as shown in Fig. 3(a). Calculated spectra for substitutions on the In(1) and In(2) sites are summed taking the site-multiplicities into account. Half of the dopants are assumed to be distributed on the In(1) sites and the remaining half on the In(2) sites. Such a distribution of dopants, which is incongruous with the site multiplicities, was confirmed in the Cd and Sn doped cases [25, 26]. For each doped supercell, the NQR lines are calculated by solving the electric quadrupole Hamiltonian $\mathcal{H}_{\mathrm{Q}} = (h\nu_{\mathrm{Q}}/6)\{3I_z^2 - I(I+1) + (\eta/2)(I_+^2 + I_-^2)\}$, with the assumption of a natural line

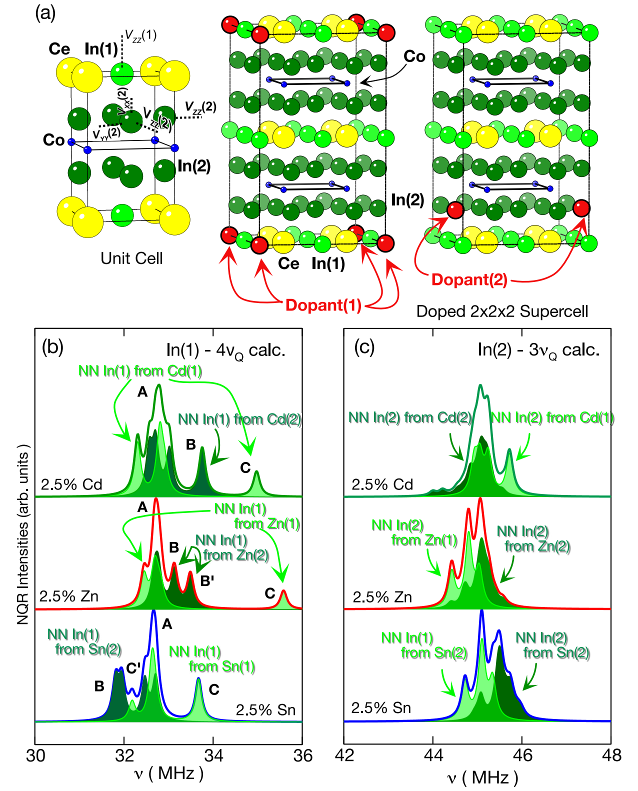

FIG. 3. (a) The unit cell and the assumed $2 \times 2 \times 2$ supercells for the doped system. The local EFG coordinations for the In(1) and In(2) sites are indicated by the dotted lines in the unit cell. Calculated spectral shapes for (b) $4\nu_{\mathrm{Q}}$ of In(1) NQR and (c) $3\nu_{\mathrm{Q}}$ of In(2) NQR for 2.5% Zn doped CeCoIn$_5$. For comparison, the results in 2.5% Cd and Sn doped cases [6] are also shown.

width of 100 kHz for the calculated EFG on every In site. To compare with experimental results, the computed spectral frequencies are multiplied by a factor of ∼0.9, to allow for screening of the EFG by conduction electrons in the real lattice. A similar approach has been reported earlier [27].

As previously reported [6], the B peaks in the 1.5% Cd and 3% Sn doped cases can be assigned to the NN In(1) sites from dopants on the In(2) sites, and the C and C' peaks to the NN In(1) sites from dopants on In(1) sites. For L (L=Sn, Cd, and Zn) dopants, dopants on the In(1) sites are labeled as $L(1)$, and those on the In(2) sites as $L(2)$. The calculations for 2.5% Zn doping can also reproduce the NQR spectral features, e.g., the In(1) NQR lines are rather discrete compared to the In(2) lines, as shown in Figs. 3(b) and 3(c). Similarly, as indicated in Fig. 3(b), the B (B') and C lines can be assigned to the NN In(1) sites from Zn(2) and Zn(1) dopants, respectively. The C subpeak could not be experimentally observed even if the frequency was swept over a wide range. This suggests that the Zn dopants preferentially occupy the In(2) sites. As for the In(2) spectra, the peak separations are not well-resolved experimentally (Fig. 2), although the simulation predicts a certain asymmetric broadening (see Fig. 3(c)).

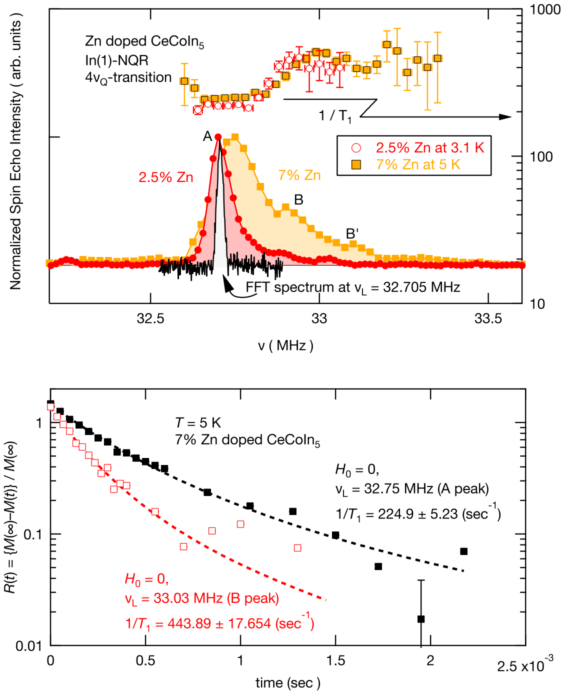

FIG. 4. (a)Frequency dependence of $1/T_1$ for the In(1) $4\nu_{\mathrm{Q}}$ line in 2.5% Zn (nominal) doped CeCoIn$_5$ at 3.1 K and in 7% Zn (nominal) doping at 5 K. In(1)–$4\nu_{\mathrm{Q}}$ NQR spectra at 3.1 K are also shown. A typical fast Fourier transform (FFT) spectrum of the spin echo signal taken at $\nu_{\mathrm{L}} = 32.705$ MHz for the 2.5% sample with the pulse condition for the T_1 measurement is superimposed, which shows the r.f. excitation frequency window. (b) Recovery curves of nuclear magnetization for the A (32.75 MHz) and B (33.03 MHz) peaks in 7% Zn-doped CeCoIn$_5$ at 5 K. The dotted curves represent fits to $R(t)$ for $I = 9/2$ NQR with the respective T_1.

To examine the difference between the electronic environments on the A and B sites, the measured frequency dependence of NQR $1/T_1$ is shown in Fig. 4(a). The nuclear magnetization recovery at each frequency was taken using the weak r.f. pulse condition to excite a narrow frequency window. For example, a typical frequency window is shown in Fig. 4 by an FFT spectrum of the spin echo signal taken at $\nu_{\mathrm{L}} = 32.705$ MHz. In Fig. 4(b), the respective recovery curves for the A and B peaks in 7% Zn doped CeCoIn$_5$ at 5 K are also shown. The data can be well fit to about 99% of full recovery for the A peak, and to at least 90% for the B peak, which means that there is no significant distribution in T_1 within each of the excited nuclear transitions. In this way, T_1 values at various temperatures and frequencies are derived. In both 2.5% and 7% Zn doping cases, as shown in Fig. 4(a), $1/T_1$ values on the main peak do not change from those in pure CeCoIn$_5$, while the values on B and B' peaks are enhanced from the bulk value. Thus, electronic correlations near the Zn(2) dopant are different from the bulk electronic state in Zn doped CeCoIn$_5$.

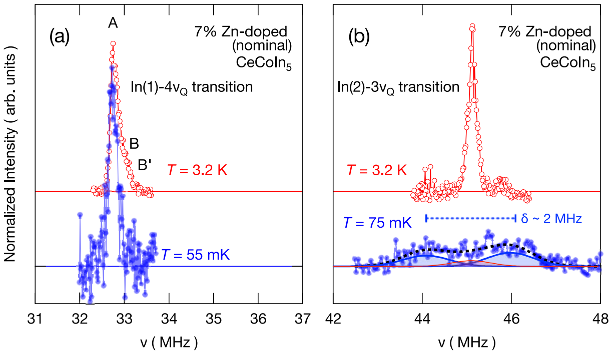

FIG. 5. (a) NQR spectral changes in 7% Zn (nominal) doped CeCoIn$_5$ under zero external field of (a) the $4\nu_Q$ transition for the In(1) sites at 4.2 K and 0.055 K, and (b) the $3\nu_Q$ transition for the In(2) sites at 2.6 K and 0.075 K.

C. The NQR/NMR spectra in the AFM state under zero field

Figure 5 shows spectral changes for the $4\nu_Q$ transition of In(1) NQR and the $3\nu_Q$ of In(2) NQR between the PM phase and the low temperature coexisting AFM and SC state of the 7% Zn doped sample. Because NQR/NMR signal intensities were significantly reduced due to Meissner shielding below T_c, the signal-to-noise ratio of the spectra in the SC+AFM state is greatly reduced relative to the PM state. In the case of In(1) NQR (Fig. 5(a)), neither splitting nor broadening is observed, indicating that the internal field is fully cancelled at the In(1) sites. Therefore, as shown later in Sec. III D, In(1) NQR is feasible for $1/T_1$ measurements through T_N and T_c.

It is expected that the hyperfine field ($H_{\rm int}$) from the ordered moments will perturb the NQR spectrum in the AFM state. This is indeed the case for In(2), where the NQR spectrum is significantly broadened below T_N (Fig. 5(b)). Because the hyperfine fields are usually several tesla, we expect that the line shape should be similar to a regular NMR spectrum acting under an internal field but zero external applied field. The In(2) NMR spectrum in the AFM+SC state mainly consists of a double-Gaussian-type shape with a separation of $\delta \sim 2$ MHz. The full line width of each Gaussian spectrum is as large as ∼1.6 MHz, reflecting an inhomogeneous distribution of internal fields on the In(2) sites. In addition, another small Gaussian-shaped peak centered at ∼45.1 MHz is required to describe the data. This corresponds to PM (SC only) regions of the sample. Since the spectral area corresponds to the volume fraction of AFM and PM (SC only) regions, we conclude that the PM (SC only) region appears to be relatively small. Similar In(2) spectra are observed in the case of 1% Cd doped CeCoIn$_5$ [23]. A similar distribution of $H_{\rm int}$ at certain muon stopping sites is also observed in μSR measurements on Cd doped CeCoIn$_5$ [28]

Both the results on the In(1) and In(2) sites suggest an in-plane commensurate AFM (C-AFM) arrangement with $\boldsymbol{q}_{\rm AFM} = (\frac{1}{2}, \frac{1}{2}, q_z)$, $(0, \frac{1}{2}, q_z)$, or $(\frac{1}{2}, 0, q_z)$ in 7% Zn doped CeCoIn$_5$. Indeed, a recent neutron scattering study in the same Zn-doped sample detects the C-AFM vector $\boldsymbol{Q}_{\rm C} = (\frac{1}{2}, \frac{1}{2}, \frac{1}{2})$ [29], which is also equivalent to that determined in 1% Cd doped CeCoIn$_5$ [30]. Interestingly, the splitting of the In(2) spectrum is closely analogous to that observed in the 1% and 1.5% Cd-doped cases [6, 23], which suggests that the size of ordered moment ($\mu_{\rm ord}$) appears to be nearly identical among those hole-doped cases.

We estimate $\mu_{\rm ord}$ to be ∼0.2–0.7 $\mu_{\rm B}$/Ce from the transferred hyperfine field $H_{\rm int}$, assuming a hyperfine coupling constant similar to that in the related AFM materials CeIn$_3$ or CeRhIn$_5$, as described below. Because the In(2) NMR spectrum is so broad in Fig. 5(b), it is difficult to determine the directions of $\mu_{\rm ord}$ in the C-AFM arrangement. Regardless of orientation of the ordered moments, the magnitude of $\mu_0 H_{\rm int}$ can be estimated to be ∼0.2–0.3 T from the exact diagonalization of $\mathcal{H}_{\rm Q} + \mathcal{H}_{\rm Z}$ where $\mathcal{H}_{\rm Z}$ is the Zeeman term. The aforementioned CeIn$_3$ exhibits a C-AFM state with a uniform moment of 0.48–0.65 $\mu_{\rm B}$/Ce [31, 32], in which the $\mu_0 H_{\rm int}$ ($\perp V_{ZZ}$) on the In sites is estimated to be ∼0.5 T [33]. On the other hand, CeRhIn$_5$ shows an incommensurate AFM (IC-AFM) spiral state with 0.54 $\mu_{\rm B}$/Ce ($\perp c$) [34], in which the amplitude of the oscillating $\mu_0 H_{\rm int}$ ($\parallel c$) is estimated to be 0.27 T [35].

The small moment, which is much smaller than that for a free Ce^{3+} ion with $g_J J = 2.16$ $\mu_{\rm B}$ (g_J: Landé g-factor, J: total electronic angular momentum), suggests an itinerant spin density wave (SDW)-type AFM order. Interestingly, the moment is similar to that observed in the so-called "Q"-phase of pure CeCoIn$_5$, where magnetic order develops inside the SC phase near the SC upper critical field H_{c2} [36].

D. ^{115}In NQR $1/T_1$ under zero field

Generally, $1/T_1$ in units of $k_{\rm B} = \hbar = 1$ can be expressed [37] as

$$\frac{1}{T_1} = 2T(\gamma_{\rm n} A_\perp)^2 \sum_{\boldsymbol{q}} f^2(\boldsymbol{q}) \frac{{\rm Im}\chi_\perp(\boldsymbol{q}, \omega_0)}{\omega_0}, \qquad (1)$$

where $f(\boldsymbol{q})$ is the hyperfine form factor (considered as unity for simplicity in most cases), ${\rm Im}\chi(\boldsymbol{q}, \omega_0)$ is the imaginary part of the dynamical susceptibility, ω_0 is the nuclear Larmor frequency, and $\perp$ refers to the component perpendicular to the quantization axis. Thus, $1/T_1$ can be regarded as a good measure of the electronic correlations.

The T dependences of $1/T_1$ on the In(1) sites in 7% Zn (nominal) doped CeCoIn$_5$ for the A and B peaks are shown in Fig. 6. For comparison, we include the data for non-doped, 2.5% Zn (nominal) doped, and 1.5% Cd

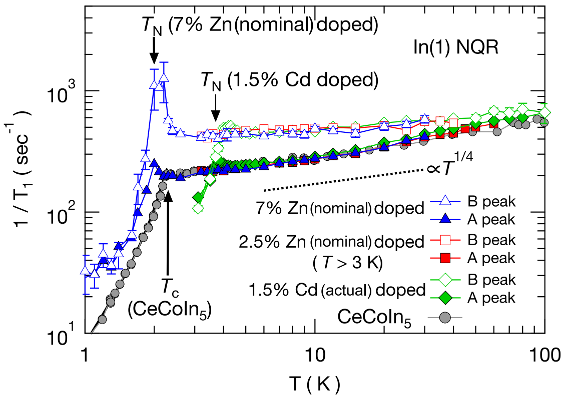

FIG. 6. Temperature dependence of $1/T_1$ for In(1) NQR measured at the A and B peaks in 7% and 2.5% Zn (nominal) doped CeCoIn$_5$. The data for the undoped and the 1.5% Cd (actual) doped CeCoIn$_5$ [6] are also shown. The dotted line represents a characteristic slope of $T^{1/4}$-dependence.

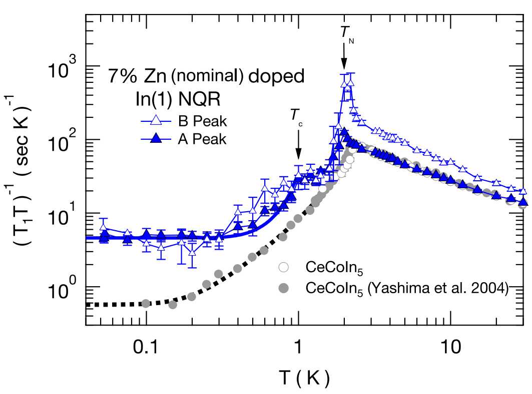

FIG. 7. Temperature dependence of $(T_1T)^{-1}$ for In(1) NQR measured at the A and B peaks in 7% Zn (nominal) doped CeCoIn$_5$. The data for CeCoIn$_5$ [38] are also shown. The thick-dotted and bold curves represent calculations assuming a dirty d-wave SC model as discussed in the text.

(actual) doped [6] CeCoIn$_5$. The data for pure CeCoIn$_5$ are consistent with the literature [38, 39]. At $T \geq 100$ K, all the $1/T_1$ data appear to coincide with those for pure CeCoIn$_5$. The crossover temperature between localized and itinerant regimes is reported to be $T^* \sim 150$ K in CeCoIn$_5$ [38].

The difference of $1/T_1$ between the A and B peaks is clearly seen below ~ 50 K $\ll T^*$. While the values and T dependence of $1/T_1$ for the A peak in the PM state are identical to those in the undoped CeCoIn$_5$, those for the B peak appear to be nearly T independent as T decreases down to $\sim T_{\rm N}$. The characteristic $T^{1/4}$–dependence of $1/T_1$ in the non-doped CeCoIn$_5$ reflects strong electronic correlations on the verge of an AFM QCP. In contrast, the T-independent $1/T_1$ for the B peak is characteristic of a fluctuation spectrum from localized $4f$ moments with a small magnitude. For the 1.5% Cd doped case, the interpretation of localized $4f$ spin dynamics surrounding the Cd(2) dopants is further corroborated over the same T range by the transverse nuclear spin relaxation rates $1/T_2$ [6, 40].

Notably, $1/T_1$ values for the B peak in the T range of $\sim T_{\rm N} < T < T^*$ do not change whether the dopant is Zn or Cd, nor do they depend on the dopants' concentration. This suggests that $1/T_1$ is locally determined by residual moments from the matrix of CeCoIn$_5$ in the neighborhood of $L(2)$ sites. In the 7% Zn doped case, $1/T_1$ for the A peak shows a small peak due to slowing-down of the spin fluctuations at $T_{\rm N}$, but $1/T_1$ for the B peak shows a large enhancement at a temperature just above $T_{\rm N}$. Such a leading peak in $1/T_1$ at a temperature just above $T_{\rm N}$ is seen for the B peak in the 1.5% Cd case as well. This indicates that the unscreened $4f$ moments in the vicinity of the Zn(2) or Cd(2) dopants nucleate long-range antiferromagnetism at $T_{\rm N}$.

Figure 7 shows $(T_1T)^{-1}$ vs T for undoped and 7% Zn doped CeCoIn$_5$ in the low temperature region. $(T_1T)^{-1}$ for the A peak rapidly decreases just below $T_{\rm N}$, and then it reaches a constant of $(T_1T)^{-1} \sim 30$ (sec K)$^{-1}$. This somewhat large $(T_1T)^{-1}$ value near $T_{\rm c}$ after opening an AFM gap indicates extra fluctuations, which may be attributed to SC fluctuations near the boundaries between A and B domains. Upon further cooling, $(T_1T)^{-1}$ shows another drop at $T_{\rm c}$, indicating the emergence of SC. As plotted together in Fig. 7, the $(T_1T)^{-1}$ in CeCoIn$_5$ shows a sudden decrease at $T_{\rm c}$=2.3 K, follows a T^2-dependence as T decreases, and finally reaches a constant value attributed to a residual density of states (DOS). The T dependence of $(T_1T)^{-1}$ can be calculated using a strong-coupling d-wave SC model with a finite DOS from impurities in the following way: To compare with literature values, an anisotropic gap function is assumed as a tentative polar function $\Delta(\theta,\phi) = \Delta_0(T)\cos\theta$, where θ and ϕ are angular parameters on the spherical Fermi surface, and $\Delta_0(T)$ is assumed to be a BCS-like function. Then, the T dependence of $1/T_1$ below $T_{\rm c}$ can be calculated from the following integral

$$\left(\frac{1}{T_1}\right)/\left(\frac{1}{T_1}\right)_{T=T_{\rm c}} = \frac{2}{k_{\rm B}T}\int\left\langle\frac{N_{\rm s}(E)^2}{N_0^2}\right\rangle_{\theta,\phi} f(E)[1-f(E)]dE,$$

where $N_{\rm s}(E)/N_0 = E/\sqrt{E^2-\Delta(\theta,\phi)^2}$ with N_0 being the DOS in the normal state, $f(E)$ is the Fermi distribution function, and $\langle\cdots\rangle_{\theta,\phi}$ means the angular average over the Fermi surface. We also include a parameter $N_{\rm res}(0)$ in the DOS $N_{\rm s}(E)$ for the SC quasiparticles to reflect the extent of gapless excitations at the Fermi level originating from strong potential scattering. [41, 42]

In CeCoIn$_5$, the calculation assuming the SC gap $2\Delta_0(0) \simeq 10k_{\rm B}T_{\rm c}$ and a small residual DOS $N_{\rm res}(0) \simeq 0.085N_0$ can reproduce the experimental data [19, 38]. On the other hand, in the 7% Zn doped case, if the same $2\Delta_0(0)$ and a large $N_{\rm res}(0) \simeq 0.45N_0$ are assumed, the calculated curve below $T_{\rm c}$ can well explain the data for the A peak in the 7% Zn doped CeCoIn$_5$, as shown in Fig. 7. Here, the normal state N_0 is determined from the

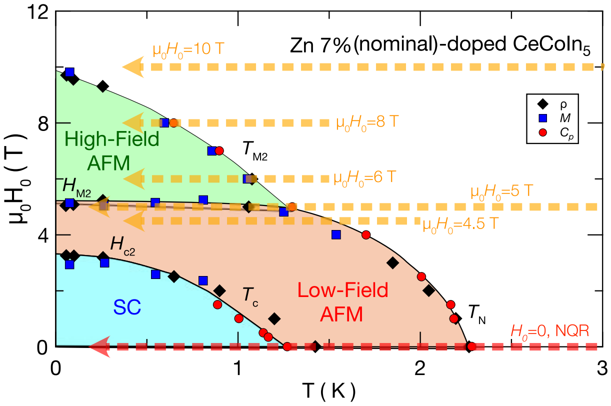

FIG. 8. H_0–T phase diagram of 7% Zn (nominal) doped CeCoIn$_5$ in the case of $H_0 \parallel c$ determined using electrical resistivity, magnetization, and specific heat measurements [16, 17]. The horizontal dotted arrows indicate the experimentally accessed temperature sweeps in this NMR and NQR ($H_0 = 0$) study.

$(T_1T)^{-1}$ value just at T_c. Thus, a SC state with the same SC gap seems to nucleate from the unchanged electronic state as in pure CeCoIn$_5$. We note that the reduction of T_c from 2.3 K to ∼1 K can be understood to be a consequence of impurity scattering, which also leads to the large residual DOS [42, 43].

On the other hand, $(T_1T)^{-1}$ for the B peak rapidly decreases at temperatures below T_N, and then it reaches a constant value of $(T_1T)^{-1} \sim 30$ (sec K)$^{-1}$ similar to that for the A peak. This implies that the Fermi liquid state, after opening the AFM gap, would be a rather homogeneous electronic state. With further decrease in T, $(T_1T)^{-1}$ for the B peak shows a gradual decrease below T_c as if transition is smeared, and $(T_1T)^{-1}$ reaches a constant value similar to that of the A peak at the lowest temperatures. It appears that the SC state is strongest away from the Zn(2) impurities, but eventually percolates through the entire sample. Notably, $(T_1T)^{-1}$ for both A and B peaks shows no upturn at the lowest temperatures, i.e., there is no signature of fluctuating local moments.

E. NMR investigation for the high field AFM phase

Recently, a new AFM state called the HF-AFM state has been observed above a critical field H_{M2} at T_{M2} using electrical resistivity, magnetization, and specific heat measurements [17]. In the magnetization curve at $T = 80$ mK, a small kink is observed at H_{M2}. A similar anomaly in the magnetic susceptibility and a small hump in the T-dependence of specific heat are also observed at T_{M2}. The H_0–T phase diagram for 7% Zn (nominal) doped CeCoIn$_5$ with $H_0 \parallel c$ [16, 17] is shown in Fig. 8. The SC H_0–T area shrinks relative to the pure compound [4], and the low-field AFM state appears and surrounds the SC phase.

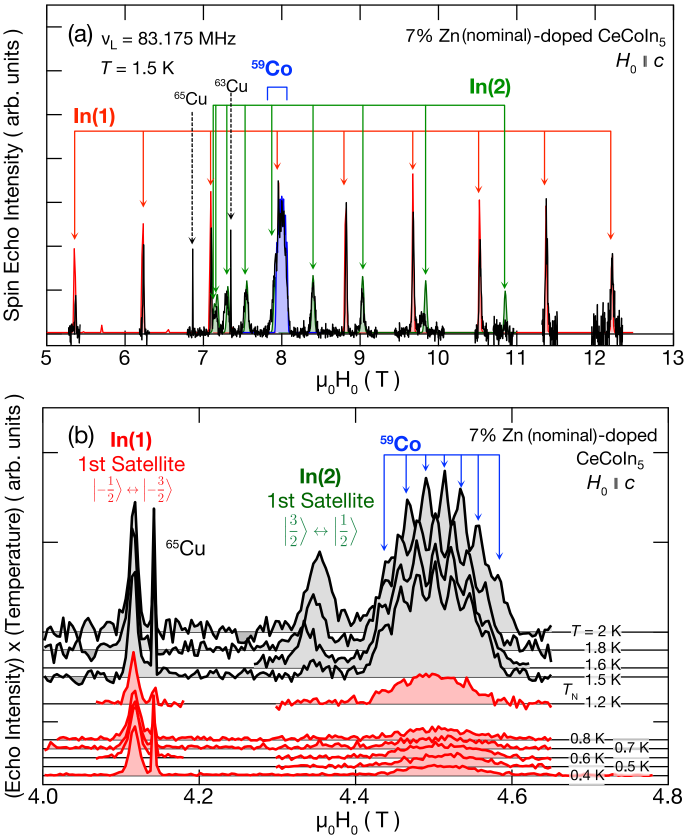

FIG. 9. (a) Full NMR spectra for 7% Zn (nominal) doped CeCoIn$_5$ in the PM state at 1.5 K (See Fig. 8 above $\mu_0 H_0 = 5$ T) in the case of $H_0 \parallel c$, taken with a constant frequency of $\nu_L = 83.175$ MHz. The spectral assignments are also indicated. (b) Temperature variation of part of NMR spectra for 7% Zn doped CeCoIn$_5$ with $H_0 \parallel c$, taken with $\nu_L = 46.77$ MHz. The AFM state below $T_N(H_0)$ corresponds to the low field AFM state. Each data is vertically shifted by the temperature. The ^{63,65} Cu-NMR lines originate from the copper r.f. coil.

We begin with field swept NMR spectra in the PM state for 7% Zn (nominal) doped CeCoIn$_5$ with $H_0 \parallel c$ (Fig. 9(a)), which are taken at 1.5 K with a constant frequency of $\nu_L = 83.175$ MHz. As indicated in Fig. 9(a), all the peaks can be successfully assigned using the respective NMR shift and NQR parameters for the nuclear sites of ^{115}In(1), ^{115}In(2), and ^{59}Co. We point out that the fine NQR structures described in Sec. III A are obscured by the larger width of each NMR line due to an inhomogeneous distribution of NMR shifts.

NMR spectral variations in the low-field AFM state are consistent with the NQR/NMR at zero field presented in Sec. III C. Namely, when H_0 is applied along the c axis, the C-AFM state with $\boldsymbol{Q}_C$ imposes no transferred field on the In(1) sites, but it does add a finite H_{int} on the In(2) sites, yielding split lines, line-broadening, and an increase of $1/T_2$ caused by inhomogeneous distribution of H_{int}. This was also as observed in zero field in Fig. 5(b).

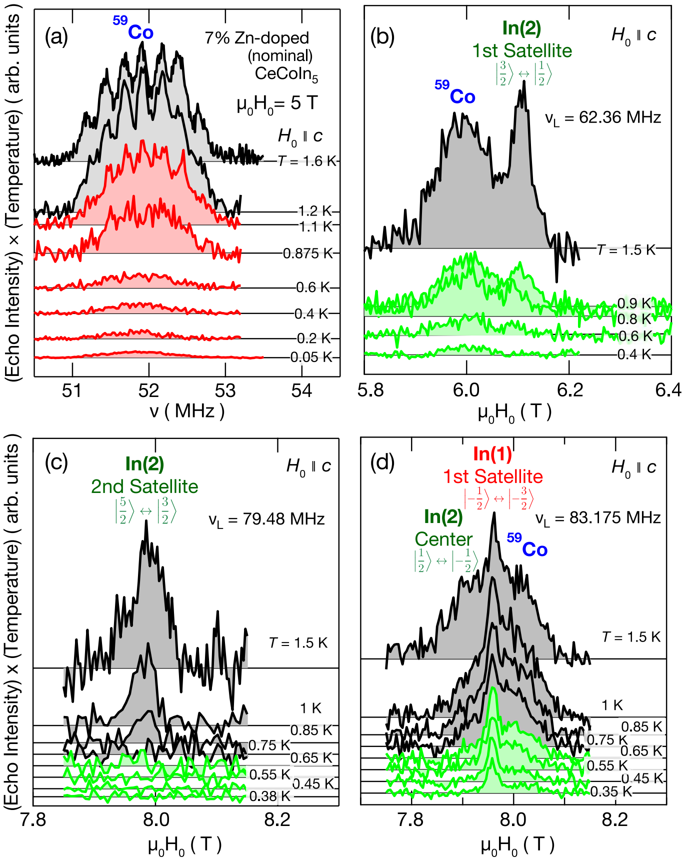

FIG. 10. (a) Temperature variation of the frequency swept ^{59}Co NMR spectrum for 7% Zn (nominal) doped CeCoIn$_5$ with applying $\mu_0 H_0 = 5$ T parallel to the c axis. Temperature variations of the field swept NMR spectra for 7% Zn doped CeCoIn$_5$ in the case of $H_0 \parallel c$ with constant frequencies of (b) $\nu_{\rm L} = 62.36$ MHz, (c) 79.48 MHz and (d) 83.175 MHz, respectively. Each data is vertically shifted by the temperature.

Therefore, as shown in Fig. 9(b), using a frequency of $\nu_{\rm L} = 46.77$ MHz, the first satellite NMR transition ($|-\frac{1}{2}\rangle \leftrightarrow |-\frac{3}{2}\rangle$) of In(1) remains unchanged below $T_{\rm N}(H_0)$ but the In(2) NMR spectra immediately disappears once magnetic order develops. Similar to In(1), the ^{59}Co NMR remains visible at the same field below $T_{\rm N}(H_0)$, as the internal field also cancels at the Co sites, although the signal intensity significantly decreases due to an increase of $1/T_2$. As shown in Fig. 10(a), near the phase boundary between the low field AFM and the HF-AFM states at $\mu_0 H_0 = 5$ T, the ^{59}Co NMR spectra for $\nu_{\rm L} = 62.36$ MHz behaves as in the low field AFM state below $T_{\rm N}$.

When the system enters the HF-AFM state, both the ^{115}In(1) and ^{59}Co NMR still remain at their PM positions, as seen in Figs. 10(b)–(d). Noteworthy are the ^{115}In(2) NMR spectra. Although the first satellite ($|\frac{3}{2}\rangle \leftrightarrow |\frac{1}{2}\rangle$) In(2) NMR spectrum disappears immediately in the low field C-AFM phase below $T_{\rm N}$ (Fig. 9(b)), it barely remains observable just below $T_{\rm M2}(H_0) \sim 1.2$ K at $\mu_0 H_0 \sim 6.1$ T, as shown in Fig. 10(b). These results mean that the In(2) spectrum has a finite spectral weight at the position of $H_{\rm int} = 0$ in the HF-AFM state. As seen in Figs. 10(c) and 10(d), however, at $\mu_0 H_0 \sim 8$ T the 2nd satellite ($|\frac{5}{2}\rangle \leftrightarrow |\frac{3}{2}\rangle$) and central ($|-\frac{1}{2}\rangle \leftrightarrow |\frac{1}{2}\rangle$) In(2) NMR are severely smeared again.

From this observation, an IC-AFM conical structure with $\boldsymbol{Q}_{\rm IC} = (\frac{1}{2}, \frac{1}{2}, q_{\rm IC})$ of $\mu_{\rm ord}$ along $\langle uvw\rangle$ is highly probable. Here, u, v, and w are arbitrary numbers, but w is introduced to account for the tilting of $\mu_{\rm ord}$ due to H_0 along the c axis, assuming $w \propto H_0$. Assuming such an IC-AFM structure, the site-to-site transferred field on In(2) sites is sinusoidally modulated from $-H_{\rm int}$ to $H_{\rm int}$, and those on In(1) and Co sites are cancelled. Consequently, it is natural to assume that $\mu_{\rm ord}$ in the low field C-AFM phase is parallel to the c axis. Namely, the critical field $H_{\rm M2}$ is a spin-flop-like transition.

Alternatively, if the magnitude of $\mu_{\rm ord}$ is modulated along the c axis, i.e., a spin-density-wave along the c axis, both the In(1) and Co NMR spectral centroids should be shifted by finite transferred fields, but such NMR shifts are not observed. As another possibility for the HF-AFM state, we consider a C-AFM with $\boldsymbol{Q}_{\rm C}$ where $\mu_{\rm ord}$ orients along $\langle uvw\rangle$. If either u or $v = 0$, no transferred field would appear on half of the In(2) sites. This case is, however, unlikely since there should be an NMR response from the half of the In(2) sites with no transferred field at low T in the HF-AFM state, which is not observed. More generally, any moment orientation $\langle uvw\rangle$ with a finite u and v and a commensurate wave vector $\boldsymbol{Q}_{\rm C}$, the hyperfine field is transferred to every In(2) sites, so this case cannot explain the partial cancellation of the hyperfine fields observed just below $T_{\rm M2}$.

Therefore, an IC-conical structure with in-plane $\mu_{\rm ord}$ canted by H_0 is more likely realized in the HF-AFM state. As discussed in the following Sec. III F, the HF-AFM state may be also heterogeneous, and the spin-flopped AFM regions gradually fade away with higher external fields ($\gg H_{\rm m2}$). Therefore, the disappearance of In(2) NMR at higher fields also would be caused by a reduction of the AFM volume.

F. Microscopic picture of the heterogeneous electronic state in Zn doped CeCoIn$_5$

Previous studies on Cd doped CeCoIn$_5$ [11, 23] proposed a “droplet” model of the AFM state. Our NQR $1/T_1$ measurement on Zn-doped material also reveals a heterogeneous electronic state in this system, equivalent with that found in Cd doped CeCoIn$_5$ [6]. The model depicts spatially confined local spins near the Zn(2) dopant in the matrix heavy fermion state.

A recent scanning tunneling microscopy (STM) study in a very dilute alloy film of CeCo(In$_{0.993}$Zn$_{0.007}$)$_5$ [44], however, has reported that the local DOS around Zn(2) sites shows little change inside the cf hybridization gap and that the SC gap spectra around the Zn dopants are essentially unchanged. Because the doping density $y =$

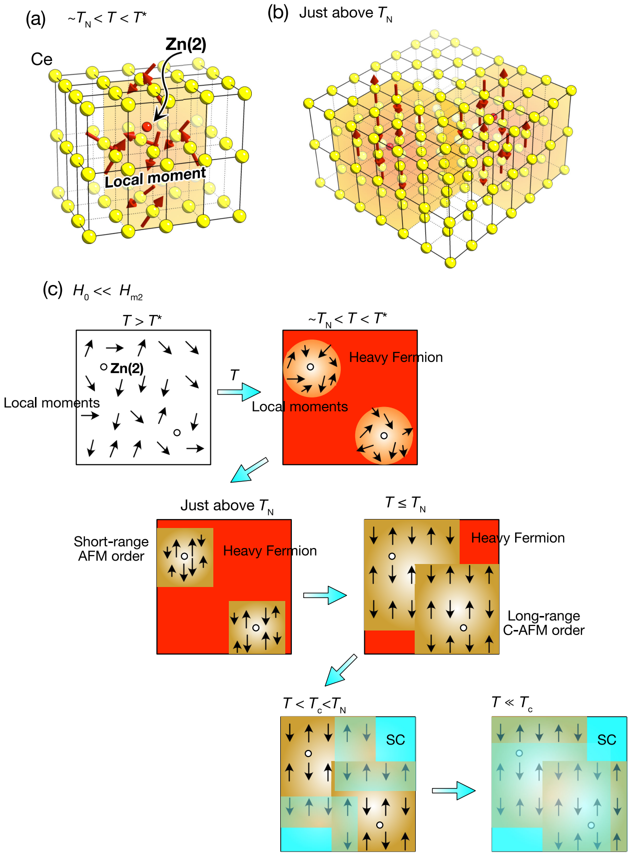

FIG. 11. Schematic illustrations of the microscopic pictures in the Zn doped CeCoIn$_5$. (a) The uncompensated local moments remain below T^* in the proximity of a Zn(2) dopant. The orange color-shaded area represents an antiferromagnetically correlated region of the local moments. (b) The percolated AFM region is viewed in a $6 \times 6 \times 2$ lattices just above T_N. (c) Schematic T-variation of the heterogeneous electronic state in fields below H_{M2}.

0.007 in the STM study is much lower than $y \sim 0.02$ in which long range AFM ordering is observed [16], we speculate that a larger chemical potential shift by denser hole-doping may be necessary for a measurable change in the local DOS to be detected by STM.

As discussed in Sec. III B, the B peak in the NQR spectra for Zn doped CeCoIn$_5$ can be assigned to the NN In(1) sites from the Zn(2) dopants, by comparison with the result from an electronic calculation of a $2 \times 2 \times 2$ superlattice. The range of sites electronically influenced by Zn(2) dopants would be spread out a bit from the 1st nearest neighbor in the actual crystal. As shown in Sec. III D, we have found a $1/T_1$ enhancement at the B peak, which is nearly T-independent, i.e., a small group of sites neighboring Zn(2) sites remains unscreened by the conduction electrons. On the other hand, the T dependence of $1/T_1$ for the bulk A sites above T_N is the same as in CeCoIn$_5$. That is, the majority of the Zn-doped sample is in the same electronic state as in undoped CeCoIn$_5$. Thus, our NQR $1/T_1$ results in the Zn doped system suggest that residual moments appear in the 1st and/or 2nd coordination sphere around the Zn(2) dopant, while most of the local $4f$ moments on Ce sites are screened well below T^* by conduction electrons through the Kondo effect. In 7% Zn (nominal) doped CeCoIn$_5$, of which the actual concentration was estimated as $y \sim 0.025$, Zn(2) would exist with a probability of 1 in ~20 unit cells, as schematically illustrated in Fig. 11(a). As T approaches T_N, the magnetic correlation length ξ_m grows to the 1st and/or 2nd coordination sphere with a diameter of $\sim$ 1–2 nm, and/or when the Zn(2) dopant induces moments out to the 3rd or 4th NN coordination sphere with a diameter of 2–5 nm. At this point, AFM domains with local order will percolate throughout the bulk, as illustrated in Fig. 11(b). As a result, long-range AFM order occurs at T_N which gives the magnetic Bragg peaks observed in a neutron diffraction experiment [29]. In the AFM state, magnetic spin-spin correlation length is estimated by the neutron scattering experiments to be $\xi_m \sim 30$ nm well below T_N in 0.75% Cd (actual) doped CeCoIn$_5$ [45] and $\xi_m \sim 10$ nm just below T_N in ~0.6% Cd (actual) doped CeCoIn$_5$ [28]. Compared with these values, our estimate of ξ_m just above T_N in 7% Zn doped CeCoIn$_5$ is reasonable.

A schematic presentation of the T-dependence of the spin structure is shown in Fig. 11(c). Outside the local AFM regions, hybridized electrons form a heavy fermion state, fundamentally equivalent to that in CeCoIn$_5$. The SC coherence length in pure CeCoIn5 is estimated as $\xi_{SC} \sim$ 5–10 nm [46] at the lowest temperature of $T \sim 50$ mK. In the alloyed compound we expect the coherence length to be smaller than in undoped CeCoIn$_5$, but still of the same order of magnitude. Thus, the SC length scale is as large as the length-scale ξ_m of AFM at the lowest temperatures, and rather smaller than ξ_m near T_c. In the AFM sphere of ξ_m, the magnetic moments are antiferromagnetically aligned and compensated. Consequently, to a Cooper pair with a short coherence length ($\xi_{SC} < \xi_m$), such AFM spheres would look like nonmagnetic impurities. Near the boundaries between AFM and heavy fermion regions, SC fluctuations would be enhanced, and then, a rather homogeneous electronic state is indicated just above T_c by NQR $1/T_1$ measurement as shown in Fig. 7. Consequently, T_c in the heavy fermion regions is lower than that in the pure material, as considered within the framework of the ‘dirty’ d-wave SC model. At the same time, when a bulk SC is established in the heavy fermion fraction of the sample well below T_c, the SC proximity effect may mask most AFM regions, like the AFM/SC proximity effect observed in Cr(SDW)/V(SC) thin films [47].

Next, let us consider the external field H_0-variation. Starting at the lowest temperature above the SC upper critical field H_{c2}, a heterogeneous state of heavy fermion and C-AFM regions is as shown in Fig. 12(a). Applying H_0 along the c axis, schematically drawn in Fig. 12(b), in-

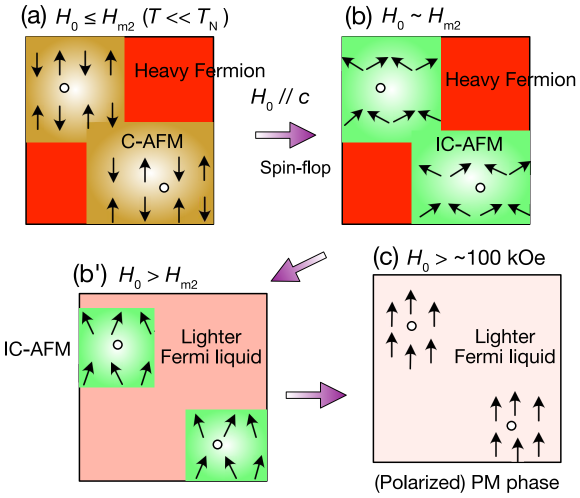

FIG. 12. Schematic H_0-variation along the c axis from (a) the low field C-AFM, via (b) (b') the high field IC-AFM states, to (c) the (polarized) PM state in the lowest temperatures for the Zn doped CeCoIn$_5$.

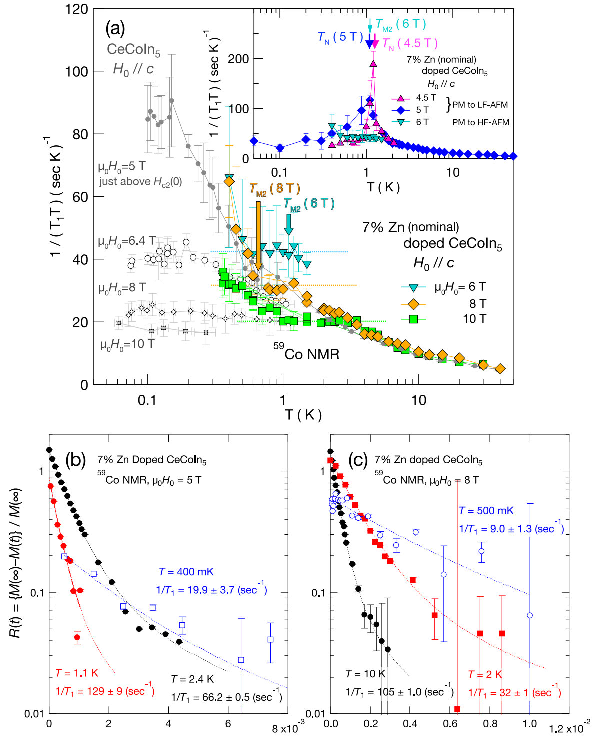

FIG. 13. (a) Temperature dependence of $(T_1T)^{-1}$ for ^{59}Co NMR in 7% Zn (nominal) doped CeCoIn$_5$ under $\mu_0H_0 = 6$, 8, and 10 T along the c axis. Data for non-doped CeCoIn$_5$ under $\mu_0H_0 = 5$, 6.4, 8, and 10 T [5] are also shown. The inset shows the $(T_1T)^{-1}$ vs T plots for ^{59}Co NMR in 7% Zn doped CeCoIn$_5$ with the applied fields of $\mu_0H_0 = 4.5$, 5, and 6 T along the c axis. (b)(c) Recovery curves of nuclear magnetization for the central transition of ^{59}Co NMR in the 7% Zn-doped material at $\mu_0H_0 = 5$ and 8 T, respectively. The dotted curves represent $R(t)$ for $I = 7/2$ NMR with the respective T_1.

duces a spin-flop-type transition at H_2 from the C-AFM region with $\mu_{\rm ord} \parallel c$, to IC conical AFM order with a component of $\mu_{\rm ord} \perp c$, as shown in Fig. 12(b). As H_0 is further increased, the AFM volume fraction and the effective mass of the heavy fermion matrix start to decrease simultaneously. (Fig. 12(b')) Above $\mu_0H_0 \simeq 10$ T, the AFM region completely disappears as illustrated in Fig. 12(c).

To confirm this microscopic picture of Zn-doped CeCoIn$_5$, we have measured $1/T_1$ for ^{59}Co NMR under several H_0. In Figs. 13(b) and 13(c), several recoveries of nuclear magnetization taken under $\mu_0H_0 = 5$ and 8 T are shown as typical examples. The data can be well fit to about 99% of full recovery in the PM state, and to about 80–90% in the magnetic phase below $T_{\rm N}$ or $T_{\rm M2}$. The obtained T_1 values in the AFM state are supposed to reflect the spatial average in the heterogeneous electronic state. The smaller values of initial recovery rate $R(0)$ at low temperatures were due to weakened r.f. pulse to avoid possible r.f. heating. It is noted that the rather large errors of T_1 below T_N or $T_{\rm M2}$ may come from the T_1 distribution between the PM and AFM portions in the heterogeneous electronic state.

The T dependences of $(T_1T)^{-1}$ for ^{59}Co NMR under several H_0 are shown in Fig. 13(a). Data for non-doped CeCoIn$_5$ [5] are included for comparison. In the PM state above ~3 K, $(T_1T)^{-1}$ for ^{59}Co NMR in non-doped and Zn doped CeCoIn$_5$ are closely matched. In the case of pure CeCoIn$_5$ with $\mu_0H_0 = 5$ T, just above $H_{c2}(0)$, $(T_1T)^{-1}$ markedly increases with decreasing temperature and reaches ~85 (sec K)$^{-1}$ at $T_{\rm FL} \sim 0.1$ K, below which it becomes T-independent. The temperature below which $(T_1T)^{-1}$ becomes constant increases with the magnetic field, but the constant value of $(T_1T)^{-1}$ decreases. These $(T_1T)^{-1}$ behaviors are well described using the self-consistent renormalized (SCR) theory for two-dimensional AFM spin fluctuations. In this scheme, the constant value of $(T_1T)^{-1}$ reflects an enhancement due to AFM spin fluctuations, as the Fermi liquid state is established below $T_{\rm FL}$. It is noted that the $(T_1T)^{-1}$ value for ^{59}Co NMR in LaCoIn$_5$ is reported to be ~0.3 (sec K)$^{-1}$ [39], which is much smaller than those in the undoped and Zn doped CeCoIn$_5$. Therefore, the $(T_1T)^{-1}$ in Fig. 13(a) mainly reflects a $4f$ contribution.

For 7% Zn doped CeCoIn$_5$, shown in the inset of Fig. 13, the T-dependence of $(T_1T)^{-1}$ at $\mu_0H_0 = 4.5$ or 5 T below $H_{\rm M2}$ peaks sharply at $T_{\rm N}(H_0)$, indicating that C-AFM order occurs. Such a peak at $T_{\rm M2}(H_0)$ is absent when crossing from PM to HF-AFM phases under $\mu_0H_0 = 6$ T above $H_{\rm M2}$. This implies that the AFM volume fraction may have decreased below the percolation threshold, that is, the HF-AFM phase may be more heterogeneous.

$(T_1T)^{-1}$ for $\mu_0H_0 = 8$ T increases gradually with decreasing T from ∼40 K, reaching a constant value of ∼30 (sec K)$^{-1}$ at approximately 2 K. The constant value of $(T_1T)^{-1}$ for $\mu_0H_0 = 6$ T is about 40 (sec K)$^{-1}$. The constant value of $(T_1T)^{-1}$ at $\mu_0H_0 = 10$ T below ∼4 K is ∼20 (sec K)$^{-1}$. This evolution of constant values of $(T_1T)^{-1}$ indicates that the effective mass of the heavy fermion region becomes lighter with increasing applied field, as schematically illustrated in Figs. 12(b') and 12(c). In contrast to a constant $(T_1T)^{-1}$ to the lowest temperatures in pure CeCoIn$_5$, $(T_1T)^{-1}$ in the Zn-doped material increases below ∼0.6–0.8 K for $\mu_0H_0 = 6, 8$, and 10 T. Such an increase in $(T_1T)^{-1}$ at the lowest temperatures is consistent with the presence of spin fluctuations coming from localized spin polarizations near the Zn dopants in the IC-AFM regions ($\mu_0H_0 = 6$ and 8 T) or in the PM phase ($\mu_0H_0 = 10$ T). Thus, the local electronic state induced by Zn dopants survives in the heavy fermion matrix even under the highest external fields.

IV. SUMMARY

The electronic state in Zn doped CeCoIn$_5$ has been investigated microscopically by means of NQR/NMR. In the NQR spectrum of the $4\nu_\mathrm{Q}$ transition for In(1) sites in 7% Zn (nominal) doped CeCoIn$_5$, satellite subpeaks appear, and from model calculations of a superlattice with Zn dopants, these subpeaks can be assigned to NN In(1) NQR near Zn(2) dopants. The In(1) and In(2) NQR spectral variations below T_N are consistent with a C-AFM structure.

The ^{115}In(1) NQR $1/T_1$ data on the main peak and the subpeak indicate a heterogeneous electronic state consisting of heavy fermion regions and spatially confined localized spins around Zn dopants. In 7% Zn (nominal) doped CeCoIn$_5$, the low-field C-AFM regions with a length scale of ∼ several lattice parameters, are nucleated near Zn(2) dopants. The C-AFM regions percolate through the bulk at T_N where the magnetic correlation length ξ_m exceeds the percolation threshold. As T decreases further, superconductivity emerges within the heavy fermion matrix below T_c. At the lowest temperatures, d-wave superconductivity permeates into AFM regions via the SC proximity effect. Thus, the AFM and SC coexistence in Zn and Cd doped CeCoIn$_5$ is a natural consequence of a real-space heterogeneous electronic state. From the In(1), In(2) and Co NMR, we find that an external field induces a spin-flop-type transition from C-AFM to the IC-conical phases. At the same time, the external field shrinks antiferromagnetically ordered regions, and AFM correlations in the heavy fermion matrix become weaker.

In such a system, a critical AFM state with $T_\mathrm{N} \simeq 0$ cannot be induced by infinitesimal hole doping, but AFM order with a finite T_N emerges suddenly only when the doping level y exceeds a certain percolation threshold. In this sense, hole-doping with Zn or Cd substitutions cannot be viewed equivalent to an effective "negative hydrostatic pressure" applied to CeCoIn$_5$. Instead, our results from Zn or Cd doped system explicitly reveal the stability of the correlated state with itinerant $4f$ electrons. Perhaps, the theoretical model [48] proposed to describe SDW order inside the SC phase of Nd doped CeCoIn$_5$ at high magnetic fields, where the Nd ions act as magnetic impurities, might be extended and applied to such a situation.

Finally, hole doping by Cd and Zn substitutions can also be viewed from another angle. Slight substitutions of Cd and Zn can easily break the c-f hybridization paths and induce spatially bound moments near the substituents, which can be regarded as voids in the heavy Fermi liquid state, i.e., Kondo holes. The spatial extent of Kondo holes and the magnitude of emergent moments appear to be universal upon hole doping CeCoIn$_5$ with Zn or Cd on the ligand site, but those holes are localized around the dopants. Certainly, the dynamics or possible mobility of Kondo holes in a quantum critical system should be further investigated, but our results also emphasize the care that needs to be taken in interpreting physical properties that assume a homogeneous response to hole doping..

ACKNOWLEDGMENTS

We are grateful for stimulating discussions with W. Higemoto, Y. Haga, R. R. Urbano, S. Seo, P. F. S. Rosa, T. Park, E. D. Bauer, and Z. Fisk. Work at Los Alamos was performed under the auspices of the US Department of Energy, Office of Science, Division of Materials Science and Engineering. DFT calculations were performed with support from the LANL LDRD program. Work at the National High Magnetic Field Laboratory was supported by the National Science Foundation Cooperative Agreement No. DMR-1644779 and the State of Florida. A part of this work was supported by JSPS KAKENHI Grant Nos. JP16KK0106, JP17K05522, JP17K05529, and JP20K03852 and by the JAEA REIMEI Research Program.

---

[1] H. v. Löhneysen, A. Rosch, M. Vojta, and P. Wölfle, Rev. Mod. Phys. **79**, 1015 (2007).
[2] G. R. Stewart, Rev. Mod. Phys. **73**, 797 (2001).
[3] E. Miranda and V. Dobrosavljević, Reports on Progress in Physics **68**, 2337 (2005).
[4] C. Petrovic, P. G. Pagliuso, M. F. Hundley, R. Movshovich, J. L. Sarrao, J. D. Thompson, Z. Fisk, and P. Monthoux, J. Phys. :Condens. Matter **13**, L337 (2001).
[5] H. Sakai, S. E. Brown, S. H. Baek, F. Ronning, E. D. Bauer, and J. D. Thompson, Phys. Rev. Lett. **107**, 137001 (2011).

[6] H. Sakai, F. Ronning, J. X. Zhu, N. Wakeham, H. Yasuoka, Y. Tokunaga, S. Kambe, E. D. Bauer, and J. D. Thompson, Phys. Rev. B **92**, 121105(R) (2015).

[7] E. D. Bauer, F. Ronning, C. Capan, M. J. Graf, D. Vandervelde, H. Q. Yuan, M. B. Salamon, D. J. Mixson, N. O. Moreno, S. R. Brown, J. D. Thompson, R. Movshovich, M. F. Hundley, J. L. Sarrao, P. G. Pagliuso, and S. M. Kauzlarich, Phys. Rev. B **73**, 245109 (2006).

[8] K. Gofryk, F. Ronning, J. X. Zhu, M. N. Ou, P. H. Tobash, S. S. Stoyko, X. Lu, A. Mar, T. Park, E. D. Bauer, J. D. Thompson, and Z. Fisk, Phys. Rev. Lett. **109**, 186402 (2012).

[9] E. D. Bauer, N. O. Moreno, D. J. Mixson, J. L. Sarrao, J. D. Thompson, M. F. Hundley, R. Movshovich, and P. G. Pagliuso, Physica B **359-361**, 35 (2005).

[10] L. D. Pham, T. Park, S. Maquilon, J. D. Thompson, and Z. Fisk, Phys. Rev. Lett. **97**, 056404 (2006).

[11] S. Seo, X. Lu, J.-X. Zhu, R. R. Urbano, N. Curro, E. D. Bauer, V. A. Sidorov, L. D. Pham, T. Park, Z. Fisk, and J. D. Thompson, Nature Physics **10**, 120 (2014).

[12] Y. Chen, W. B. Jiang, C. Y. Guo, F. Ronning, E. D. Bauer, T. Park, H. Q. Yuan, Z. Fisk, J. D. Thompson, and X. Lu, Phys. Rev. Lett. **114**, 146403 (2015).

[13] K. Chen, F. Strigari, M. Sundermann, Z. Hu, Z. Fisk, E. D. Bauer, P. F. S. Rosa, J. L. Sarrao, J. D. Thompson, J. Herrero-Martin, E. Pellegrin, D. Betto, K. Kummer, A. Tanaka, S. Wirth, and A. Severing, Phys. Rev. B **97**, 045134 (2018).

[14] N. Maksimovic, T. Cookmeyer, J. Rusz, V. Nagarajan, A. Gong, F. Wan, S. Faubel, I. M. Hayes, S. Jang, Y. Werman, P. M. Oppeneer, E. Altman, and J. G. Analytis, Evidence for freezing of charge degrees of freedom across a critical point in cecoin$_5$ (2020), arXiv:2011.12951 [cond-mat.str-el].

[15] M. Yokoyama, K. Fujimura, S. Ishikawa, M. Kimura, T. Hasegawa, I. Kawasaki, K. Tenya, Y. Kono, and T. Sakakibara, Journal of the Physical Society of Japan **83**, 033706 (2014), https://doi.org/10.7566/JPSJ.83.033706.

[16] M. Yokoyama, H. Mashiko, R. Otaka, Y. Sakon, K. Fujimura, K. Tenya, A. Kondo, K. Kindo, Y. Ikeda, H. Yoshizawa, Y. Shimizu, Y. Kono, and T. Sakakibara, Phys. Rev. B **92**, 184509 (2015).

[17] M. Yokoyama, H. Mashiko, R. Otaka, Y. Oshima, K. Suzuki, K. Tenya, Y. Shimizu, A. Nakamura, D. Aoki, A. Kondo, K. Kindo, S. Nakamura, and T. Sakakibara, Phys. Rev. B **95**, 224425 (2017).

[18] E. Bauer, D. Mixson, F. Ronning, N. Hur, R. Movshovich, J. Thompson, J. Sarrao, M. Hundley, P. Tobash, and S. Bobev, Physica B: Condensed Matter **378-380**, 142 (2006), proceedings of the International Conference on Strongly Correlated Electron Systems.

[19] Y. Kohori, Y. Yamato, Y. Iwamoto, T. Kohara, E. D. Bauer, M. B. Maple, and J. L. Sarrao, Phys. Rev. B **64**, 134526 (2001).

[20] P. Blaha, K. Schwarz, G. Madsen, D. Kvasnicka, and J. Luitz, *WIEN2K, An Augmented Plane Wave + Local Orbitals Program for Calculating Crystal Properties*, Tech. Rep. (Techn. Universität Wien, Austria, 2001).

[21] J. P. Perdew, K. Burke, and M. Ernzerhof, Phys. Rev. Lett. **77**, 3865 (1996).

[22] J. Chepin and J. J. H. Ross, J. Phys. :Condens. Matter **3**, 8103 (1991).

[23] R. R. Urbano, B. L. Young, N. J. Curro, J. D. Thompson, L. D. Pham, and Z. Fisk, Phys. Rev. Lett. **99**, 146402 (2007).

[24] E. G. Moshopoulou, J. L. Sarrao, P. G. Pagliuso, N. O. Moreno, J. D. Thompson, Z. Fisk, and R. M. Ibberson, Applied Physics A (Suppl.) **74**, 895 (2002).

[25] M. Daniel, E. D. Bauer, S. W. Han, C. H. Booth, A. L. Cornelius, P. G. Pagliuso, and J. L. Sarrao, Phys. Rev. Lett. **95**, 016406 (2005).

[26] C. H. Booth, E. D. Bauer, A. D. Bianchi, F. Ronning, J. D. Thompson, J. L. Sarrao, J. Y. Cho, J. Y. Chan, C. Capan, and Z. Fisk, Phys. Rev. B **79**, 144519 (2009).

[27] J. Rusz, P. M. Oppeneer, N. J. Curro, R. R. Urbano, B.-L. Young, S. Lebègue, P. G. Pagliuso, L. D. Pham, E. D. Bauer, J. L. Sarrao, and Z. Fisk, Phys. Rev. B **77**, 245124 (2008).

[28] L. Howald, E. Stilp, P. D. de Réotier, A. Yaouanc, S. Raymond, C. Piamonteze, G. Lapertot, C. Baines, and H. Keller, Scientific Reports **5**, 12528 (2015).

[29] M. Yokoyama and S. Raymond, Neutron scattering study for Zn-doped CeCoIn$_5$, presented at JPS Autumn Meeting (Doshisha Univ., Kyoto, Japan) (2018).

[30] M. Nicklas, O. Stockert, T. Park, K. Habicht, K. Kiefer, L. D. Pham, J. D. Thompson, Z. Fisk, and F. Steglich, Phys. Rev. B **76**, 052401 (2007).

[31] A. Benoit, J. K. Boucherle, P. Convert, J. Flouquet, J. Palleau, and J. Schweizer, Solid State Commun. **34**, 293 (1980).

[32] J. M. Lawrence and S. M. Shapiro, Phys. Rev. B **22**, 4379 (1980).

[33] Y. Kohori, Y. Inoue, T. Kohara, G. Tomka, and P. C. Riedi, Physica B **259-261**, 103 (1999).

[34] D. M. Fobes, E. D. Bauer, J. D. Thompson, A. Sazonov, V. Hutanu, S. Zhang, F. Ronning, and M. Janoschek, Journal of Physics: Condensed Matter **29**, 17LT01 (2017).

[35] N. J. Curro, P. C. Hammel, P. G. Pagliuso, J. L. Sarrao, J. D. Thompson, and Z. Fisk, Phys. Rev. B **62**, R6100 (2000).

[36] M. Kenzelmann, T. Strässle, C. Niedermayer, M. Sigrist, B. Padmanabhan, M. Zolliker, A. D. Bianchi, R. Movshovich, E. D. Bauer, J. L. Sarrao, and J. D. Thompson, Science **321**, 1652 (2008).

[37] T. Moriya, J. Phys. Soc. Jpn. **18**, 516 (1963).

[38] M. Yashima, S. Kawasaki, Y. Kawasaki, G.-q. Zheng, Y. Kitaoka, H. Shishido, R. Settai, Y. Haga, and Y. Ōnuki, J. Phys. Soc. Jpn. **73**, 2073 (2004).

[39] Y. Kawasaki, S. Kawasaki, M. Yashima, T. Mito, G.-q. Zheng, Y. Kitaoka, H. Shishido, R. Settai, Y. Haga, and Y. Ōnuki, J. Phys. Soc. Jpn. **72**, 2308 (2003).

[40] H. Sakai, F. Ronning, T. Hattori, Y. Tokunaga, S. Kambe, J. X. Zhu, N. Wakeham, H. Yasuoka, E. D. Bauer, and J. D. Thompson, J. Phys.: Conf. Ser. **807**, 032001 (2017).

[41] S. Schmitt-Rink, K. Miyake, and C. M. Varma, Phys. Rev. Lett. **57**, 2575 (1986).

[42] T. Hotta, J. Phys. Soc. Jpn. **62**, 274 (1993).

[43] Y. Kitaoka, K. Ishida, and K. Asayama, J. Phys. Soc. Jpn. **63**, 2052 (1994).

[44] M. Haze, Y. Torii, R. Peters, S. Kasahara, Y. Kasahara, T. Shibauchi, T. Terashima, and Y. Matsuda, J. Phys. Soc. Jpn. **87**, 034702 (2018).

[45] S. Nair, O. Stockert, U. Witte, M. Nicklas, R. Schedler,

K. Kiefer, J. D. Thompson, A. D. Bianchi, Z. Fisk, S. Wirth, and F. Steglich, Proceedings of the National Academy of Sciences **107**, 9537 (2010), https://www.pnas.org/content/107/21/9537.full.pdf.

[46] L. DeBeer-Schmitt, C. D. Dewhurst, B. W. Hoogenboom, C. Petrovic, and M. R. Eskildsen, Phys. Rev. Lett. **97**, 127001 (2006).

[47] M. Hübener, D. Tikhonov, I. A. Garifullin, K. Westerholt, and H. Zabel, Journal of Physics: Condensed Matter **14**, 8687 (2002).

[48] S.-Z. Lin and J.-X. Zhu, Phys. Rev. B **96**, 224502 (2017).